International Forum on Aeroelasticity and Structural Dynamics
IFASD 2019
9-13 June 2019, Savannah, Georgia, USA

QUANTIFICATION OF NONLINEAR EFFECTS IN GUST LOAD PREDICTION

Christoph Kaiser[1], **David Quero**[1], **Jens Nitzsche**[1]

[1]DLR - German Aerospace Center
Institute of Aeroelasticity
Bunsenstr. 10, 37073 Göttingen, Germany
christoph.kaiser@dlr.de

Keywords: aeroelasticity, load prediction, nonlinear CFD, time-linearized CFD, gust encounter, transonic flow, NASA common research model

Abstract: In this paper the quantification of nonlinear effects in the gust load prediction of transport aircraft configurations is addressed. Therefore, multi-disciplinary simulations of unsteady gust encounters are carried out based on Reynolds Averaged Navier-Stokes solutions. Nonlinear aeroelastic gust load analysis employing the Force Summation Method is conducted for the NASA Common Research Model at transonic speed. Additionally, gust loads based on time-linearized CFD are obtained for comparison with the nonlinear loads. Multiple discrete 1-cos gust profiles with different gust amplitudes and gust lenghts are investigated for the analysis of nonlinear effects like the existence of recompression shocks.

1 INTRODUCTION

The aircraft design and certification process demands the load analysis for a huge parameter space, including gust load analysis. Therefore, unsteady aerodynamic and aeroelastic data has to be obtained by numerical methods rendering their computational effort crucial for the aircraft design process.

A common method used for predicting unsteady airloads is the doublet-lattice method (DLM) which is based on the compressible acceleration potential theory [1]. It provides good computational efficiency but cannot account for the wing thickness or nonlinear effects of the flow as it occurs in the transonic regime such as the existence of recompression shocks and boundary layer separation. Higher-fidelity methods involving nonlinear multi-disciplinary simulations based on Reynolds Averaged Navier-Stokes (RANS) solutions require many computational resources. Hence, more efficient methods are developed based on reduced order models of the aeroelastic aircraft model. One approachis based on the time-linearized RANS equations which allows conducting the aeroelastic coupling in the frequency domain with reduced computational effort. This approach is well suited for inherently linear problems like the determination of the flutter stability by forced-motion simulations [2]. In contrast, gust load prediction requires to consider large flow perturbations which cause nonlinear flow responses. However, conservative results usually are expected from the time-linearized approach for gust profiles as they are required in the design process. The validity of the time-linearized gust approach is shown in [3] and [4] in the limit of small gust amplitudes. The time-linearized approach is recently employed in industrial context [5]. Furthermore, this approach can ease the design of the flight control system and gust load alleviation strategies.

This paper addresses the nonlinearities in the flow response caused by gust encounters on a typical transport aircraft configuration. Therefore, gust profiles of different amplitudes and gust lengths are sampled systematically from the gust parameter space. These include gust profiles as required for the certification process by the CS-25 [6]. Subsequently, a detailed loads analysis is carried out accompanied by time-linearized loads analysis in order to quantify the nonlinear effects on the predicted gust loads. The load analysis considers the aerodynamic and inertial forces of the free-flying flexible aircraft for which the aircraft's primary motion due to a vertical gust encounter is modelled by the heave and pitch motion and the first wing bending. Moreover, the effect of the gust encounter on the recompression shock which occurs in the transonic regime is investigated.

2 NUMERICAL METHODS

2.1 Aeroelastic Governing Equations

The aeroelastic governing equations can be formulated as the second-order, linear equations of motion coupled with the aerodynamic forces. The equations can be expressed for the dynamic displacements $\mathbf{x}(t)$ around the steady displacements $\bar{\mathbf{x}}$ by subtracting the steady state from the equations:

$$\mathbf{M}_{gg}\ddot{\mathbf{x}}(t) + \mathbf{K}_{gg}\mathbf{x}(t) = \mathbf{H}_{ga}\mathbf{f}_a(t), \tag{1}$$

where $\mathbf{M}_{gg}$ and $\mathbf{K}_{gg}$ are the mass matrix and stiffness matrix for the structural degrees of freedom. The aerodynamic forces $\mathbf{f}_a$ acting on the structure are transfered from the aerodynamic coordinates onto the structural coordinates by the spline matrix $\mathbf{H}_{ga}$. Eq. (1) can be transformed in terms of generalized coordinates by the matrix of eigenvectors $\mathbf{\Phi}_{gh}$ which is obtained by modal analysis of the structure in vacuum. The dynamic displacements are then $\mathbf{x}(t) = \mathbf{\Phi}_{gh}\mathbf{q}(t)$ and the system of equations is projected by multiplying with $\mathbf{\Phi}_{gh}^T$:

$$\mathbf{M}\ddot{\mathbf{q}}(t) + \mathbf{K}\mathbf{q}(t) = \mathbf{\Phi}_{gh}^T\mathbf{H}_{ga}\mathbf{f}_a(t) = \mathbf{f}(t), \tag{2}$$

with the generalized mass matrix $\mathbf{M}$, generalized stiffness matrix $\mathbf{K}$, the generalized dynamic displacements $\mathbf{q}$ and the generalized aerodynamic forces (GAF) $\mathbf{f}$. This transformation allows to reduce the number of degrees of freedom to a selected set of eigenmodes of the structural system. Eq. (2) comprise both the rigid-body motion and elastic mode shapes and therefore, it couples the disciplines of aerodynamics, structural dynamics and flight mechanics. For the investigated gust encounters in this paper, only the x-z symmetric rigid-body and elastic modes must be considered for a symmetric longitudinal flight with vertical gust encounters.

Eq. (2) is integrated in time in a staggered co-simulation applying the Newmark-β method [7] with a predictor-corrector scheme. At each time step, the generalized aerodynamic forces are extrapolated in time in order to predict the generalized displacements of the next time step. These displacements are applied in a moving-grid CFD simulation for solving for the aerodynamic forces. In the corrector step, the displacements are updated according to these forces.

The CFD simulations are performed with the DLR TAU-Code [8] in the multi-disciplinary simulation framework FlowSimulator [9]. The DLR TAU-Code solves the unsteady Reynolds-Averaged Navier-Stokes equations with an unstructured finite volume discretization. For the turbulence closure, the one-equation Spalart-Allmaras turbulence model [10] is used in this paper. The unsteady simulations are performed with the dual time stepping scheme by Jameson

[11] and second-order backward-differencing in time. For moving-grid simulations, the DLR TAU-Code includes the Arbitrary Langrangian-Eulerian (ALE) extension [12] and the surface grid movement is propagated into the volume grid by radial basis function [13]. The ALE also allows including the Field Velocity Method to introduce an independent time-varying velocity field for representing a moving gust field [14].

The section loads recovery is performed by the Force Summation Method (FSM) [15] which can be expressed as:

$$\Delta\mathbf{L}_{FSM}(t) = \mathbf{T}_{cg}(\mathbf{H}_{ga}\mathbf{f}_a(t) - \mathbf{M}_{gg}\mathbf{\Phi}_{gh}\ddot{\mathbf{q}}(t)), \tag{3}$$

where $\mathbf{T}_{cg}$ is the matrix which integrates the aerodynamic forces and the inertial forces at several monitoriing stations, e.g. on the loads reference axes, in order to compute the sectional forces in the structure. Since only the dynamic displacements and forces around the steady state are considered in Eq. (1) and Eq. (2), the predicted loads in Eq. (3) will only include the dynamic offset which is indicated by $\Delta\mathbf{L}_{FSM}$.

2.2 Time-Linearized Aeroelastic Coupling

The time-linearized aeroelastic governing equations are obtained by transforming Eq. (2) into the frequency domain setting a harmonic motion $\mathbf{q}(t) = \hat{\mathbf{q}}e^{i\omega t}$:

$$-\omega^2\mathbf{M}\hat{\mathbf{q}}(\omega) + \mathbf{K}\hat{\mathbf{q}}(\omega) = \mathbf{\Phi}_{gh}^T\mathbf{H}_{ga}\hat{\mathbf{f}}_a(\omega) = \hat{\mathbf{f}}(\omega) = \mathbf{A}(\omega)\hat{\mathbf{q}}(\omega), \tag{4}$$

with the time-linearized and harmonic generalized aerodynamic forces expressed by the GAF matrix $\mathbf{A}$ multiplied by the dynamic displacement amplitudes $\hat{\mathbf{q}}$. Hence, the GAF matrix is the transfer function matrix for the time-linearized aerodynamic system, cf. Fig. 1. It is comprised of the transfer functions for each generalized coordinate with the aerodynamic forces projected onto the generalized coordinates by $\mathbf{\Phi}_{gh}^T\mathbf{H}_{ga}$. Additionally, for considering the gust excitation, the GAF matrix is extended by an additional column with the vertical gust transfer function of the aerodynamic forces. In this work, the transfer functions are obtained by system identification [3] [16]. The linear, time-invariant aerodynamic system is virtually found for the nonlinear system around a steady state, if the excitations are of very small amplitude. In this limit, it is possible to identify the transfer function for a reasonable frequency bandwidth, by applying a broadband excitation signal $\delta(t)$ in order to approximate the impulse response. Thus, the transfer function G of the linear, time-invariant system is found by dividing the frequency response Y by the Fourier transformed excitation signal U:

$$G(\omega) = \frac{Y_\delta(\omega)}{U_\delta(\omega)}. \tag{5}$$

An interpolation method for the complex-valued transfer functions provides the evaluation of the assembled GAF matrix $\mathbf{A}(\omega)$ at additional frequencies which may be required in the following time-linearized aeroelastic coupling. The interpolation is done separately for the real and imaginary part employing cubic splines.

The time-linearized aeroelastic coupling can be represented by a feedback loop in the frequency domain, see Fig. 2. Thus, Eq. (4) can be solved for the generalized forces and displacements in the presence of a gust excitation signal $\mathbf{q}_{gust}$ by:

$$\hat{\mathbf{f}}(\omega) = \left(\mathbf{I} - \mathbf{A}\left(\omega\right)\mathbf{S}\left(\omega\right)\right)^{-1}\mathbf{A}\left(\omega\right)\hat{\mathbf{q}}_{gust}\left(\omega\right), \tag{6}$$

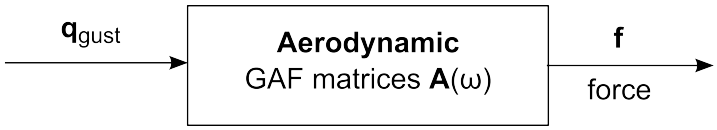

Figure 1: Aerodynamic system in the frequency domain with gust excitation.

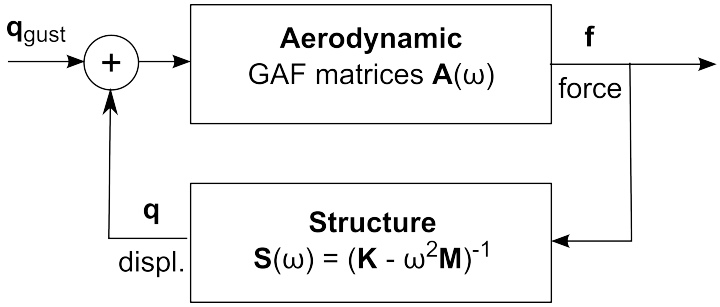

Figure 2: Aeroelastic feedback loop in the frequency domain with gust excitation.

$$\hat{\mathbf{q}}(\omega) = \left(\mathbf{S}^{-1}(\omega) - \mathbf{A}(\omega)\right)^{-1} \mathbf{A}\left(\omega\right) \hat{\mathbf{q}}_{gust}\left(\omega\right), \tag{7}$$

with

$$\mathbf{S}(\omega) = (-\omega^2\mathbf{M} + \mathbf{K})^{-1}. \tag{8}$$

The aeroelastic frequency responses obtained by Eq. (6) and Eq. (7) can then be transformed into the time domain by applying the inverse Fourier transform, provided the signals are absolutely integrable.

For computing the time-linearized loads by employing Eq. (3), the transfer functions $\mathbf{A}_a$ of the aerodynamic forces are required in terms of the aerodynamic coordinates instead of the generalized coordinates in order to obtain the aerodynamic force distribution. Therefore, Eq. (5) has to be applied for each force of the aerodynamic coordinates. Then, the solution of Eq. (7) together with the gust excitation spectrum gives the time-linearized aerodynamic force distribution in the frequency domain:

$$\hat{\mathbf{f}}_a(\omega) = \mathbf{A}_a(\omega)(\hat{\mathbf{q}}(\omega) + \hat{\mathbf{q}}_{gust}(\omega)). \tag{9}$$

Hence, the time-linearized loads are given by:

$$\Delta\mathbf{L}_{FSM}(\omega) = \mathbf{T}_{cg}(\mathbf{H}_{ga}\mathbf{A}_a(\omega)(\hat{\mathbf{q}}(\omega) + \hat{\mathbf{q}}_{gust}(\omega)) + \omega^2\mathbf{M}_{gg}\mathbf{\Phi}_{gh}\hat{\mathbf{q}}(\omega)). \tag{10}$$

3 RESULTS

3.1 Numerical Model

The transport aircraft configuration used in the following investigations is the NASA Common Research Model (CRM) [17] together with the FERMAT structural model and the C2 mass case [18]. The aerodynamic CFD model stemming from 4th AIAA Drag Prediction Workshop [19] is a half-model without a vertial tailplane and a nacelle, see Fig. 3a. The hybrid unstructured-structured volume mesh consists of around 3.7 million grid points and 100014 surface nodes. The outer boundary conditions are a farfield hemisphere with a radius of 757m and symmetric boundary conditions in the x-z symmetry plane.

The selected flight point is at the cruise Mach number of 0.86 at an altitude of 9133m. The flight shape is trimmed at an angle of attack of 1.641deg. The steady state parameters are summarized in Table 1. In Fig. 3b, the steady pressure distribution shows recompression shocks over main parts of the wing revealing the transonic nature of this steady flow condition.

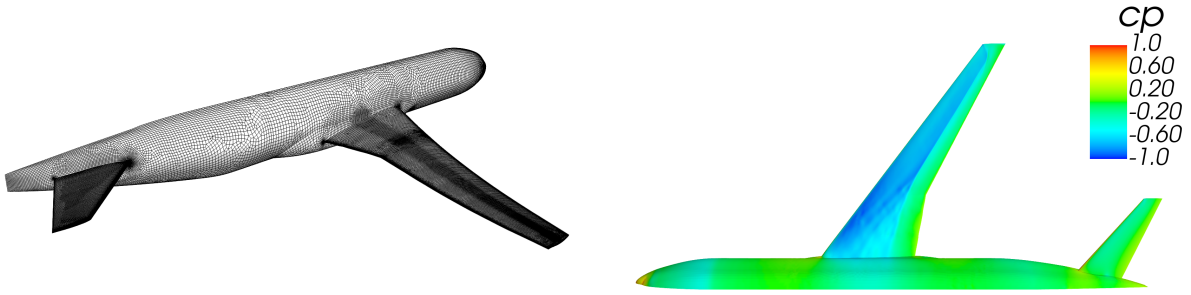

(a) Surface grid of the flight shape

(b) Pressure distribution on the upper side

Figure 3: CFD grid and steady flow state of the CRM.

Parameter	Value
Mach number	0.86
Velocity U_{ref}	260.71 m/s
Angle of attack	1.641 deg
Density	0.4588 $\mathrm{kg/m^3}$
Reynolds number	$56.3 \cdot 10^6$
Reference length L_{ref}	7 m

Table 1: Parameters of the steady flow state.

From the modal analysis of the structural model the first three x-z symmetric mode shapes are considered for representing the rigid-body and elastic motion of the aircraft. Table 2 lists the eigenfrequencies and modal scaling of the eigenmodes. The generalized aerodynamic forces obtained from the above half model are doubled in the modal coupling of Eq. (2) in order to account for the mirrored second half of the aerodynmic model.

Mode	Description	Modal Mass	Eigenfrequency
3	Heave	$2.6 \cdot 10^5$ kg	0.0
5	Pitch	$2.58 \cdot 10^7$ $\mathrm{kgm^2}$	0.0
7	First wing bending	1	1.057 Hz

Table 2: Parameters of the structural model.

The investigated gust encounters are discrete 1-cos vertical gusts propagating with the steady state velocity through the aerodynamic grid. The gust profile is defined by the gust length λ and the gust amplitude w_g. Fig. 4 shows the investigated parameter samples with gust lenghts ranging from 18m up to 210m and gust amplitudes from 0.625m/s to 20m/s resulting in a total of 39 different gust profiles. The investigated gust amplitudes correspond to gust angles of incidence $\alpha_g = \arctan(w_g/U_{ref})$ from 0.14deg to 4.38deg. For reference, the combinations of gust length and amplitude as stated in the Certification Specifications for Large Aeroplanes (CS-25) for this flight level are also shown (with a flight profile alleviation factor of 1) [6].

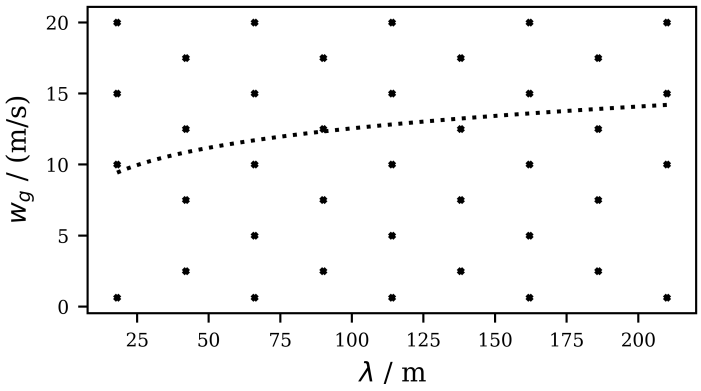

Figure 4: Investigated gust parameters (dots). For comparison, gusts as specified by CS-25 (dotted line).

3.2 Nonlinear Aeroelastic Gust Loads

Nonlinear aeroelastic gust encounters of the CRM are simulated in the time domain for several discrete 1-cos gust encounters as depicted in Fig. 4. The first three structural mode shapes are considered for describing the primary aircraft motion due vertical gust encounters: the heave and pitch motion plus the first elastic mode corresponding to the wing bending. All simulations are performed with a time step size of 0.0013s and 100 inner pseudo iterations up to a simulation period of 3s. This setup proved to produce converged results by varying the time step size. The time integration is conducted following section 2.1 with the steady state subtracted from the equations of motions in order to account for the dynamic offset only.

Fig. 5 shows the time signals of the GAFs for the gust amplitudes of 10m/s and 15m/s with five different gust lengths. The signals show qualitatively comparable results for both amplitudes. The case of 15m/s results in significantly higher forces and steeper gradients. For both cases, it can be observed that the highest GAFs occur for the mid-sized gust lengths. Furthermore, the gust length with the maximal forces may change with increasing gust ampltiude as it can be seen for the minimum bending force for a gust length of 66m. In combination with the steeper gradients, this displays the presence of some nonlinearity with increasing gust amplitude.

From the loads recovery analysis, cf. Eq. (3), the loads envelope can be extracted by taking the maximum and minimal loads at each station over time. Thus, the loads envelopes describe the limits of the loads while the aircraft is encountering the gust. Fig. 6 shows the load envelopes of the wing bending moment ΔM_x for the gust amplitudes of 10m/s and 20m/s and multiple gust lengths. The magnitude of the maximum and minimum loads increase with increasing gust lengths. However, the greatest minimum loads are reached for the gust length of 162m. With increasing gust amplitude the loads increase nonlinearly. For greater values of the gust length the increase is attenuated than for lower values. Moreover, the maximum loads shift more inboard of the wing with increasing gust amplitude.

In Fig. 7 the maximum and minimal wing bending moments at the wing root are shown as a contour plot. The values are obtained for all gusts, cf. Fig. 4, and the values in between the samples are interpolated by radial basis functions. A distinct maximum is found for the maximum load with increasing gust amplitude and gust length. In contrast, the maximum magnitude for the minimum load is not located at the greatest gust length but at 160m. Thus, Fig. 7 confirms the findings obtained above from the loads envelopes.

Fig. 8 shows the surface pressure distribution along a cut of the wing at $y = 14.5$m (50% of

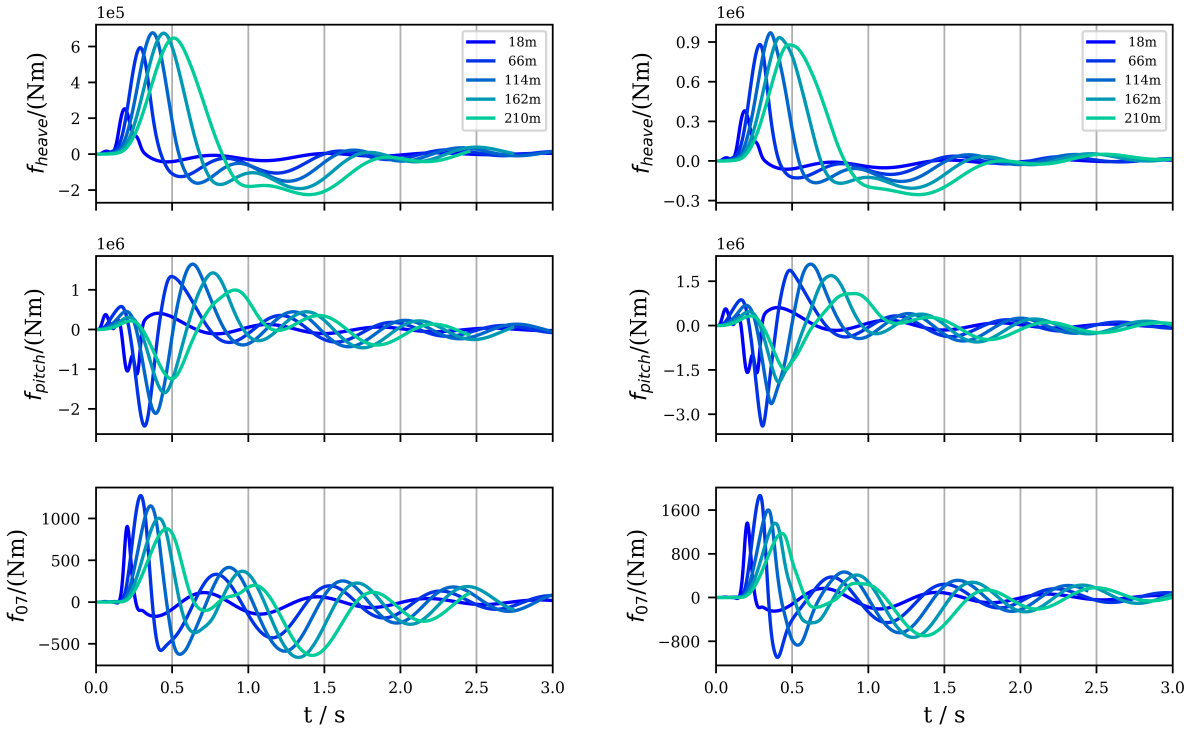

(a) $w_g = 10$m/s (b) $w_g = 15$m/s

Figure 5: Time signals of GAFs due to 1-cos gust encounters for different gust lengths.

the span). The time series of c_p is depicted together with the steady state distribution for gust amplitudes of 5m/s and 10m/s with corresponding incidences of 1.1deg and 2.2deg and gust lengths of 66m and 162m. The steady state shows a recompression shock at $x = 38$m as it is seen in Fig. 3b. For all four cases, the distribution changes from the steady state and it returns to the steady after the gust has passed the aircraft. At first, the pressure on the upper surface decreases corresponding to a velocity increase. On the lower surface the pressure increases in a less magnitude that the decrease on the upper surface yielding a higher pressure difference than in the steady state. On the upper surface, the shock moves further downstream gaining in strength, then it reverses the direction moving upstream with decreased strength. The shock position passes the steady state position to reverse its moving direction again. The velocity and the range of the shock's motion decrease with time and after some oscilations, the shock position returns to the steady state. This behaviour is comparable to an upward pitching airfoil with a regular shock motion. With increasing gust amplitude the shock motion increases and the pressure difference amplifies further. Increasing the gust length results in a greater upstream shock movement.

3.3 Comparison with Time-Linearized Aeroelastic Gust Loads

The time-linearized gust simulations are performed following the procedure described in section 2.2 for the gusts cases depicted in Fig. 4. Therefore, time-domain simulations with the broadband pulse-like excitation are conducted in order to identify the time-linearized GAF matrix in the frequency domain. Thus, the transfer functions for the generalized coordinates (heave, pitch and first wing bending) and the vertical gust encounter are determined by the ratio of the frequency reponse to the Fourier transformed excitation signal, see Eq. 5. Consequently, the transfer function matrices for the GAFs, the generalized displacements, the surface pressure

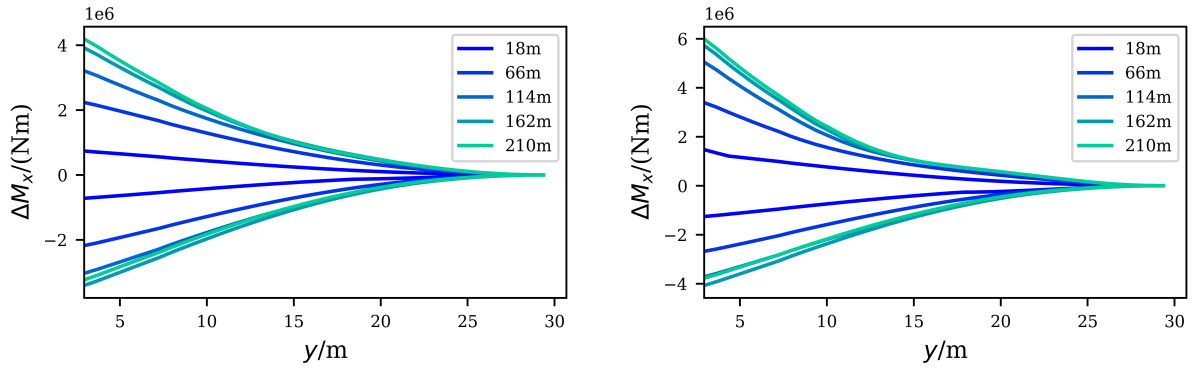

(a) $w_g = 10$m/s (b) $w_g = 20$m/s

Figure 6: Loads envelopes of the wing bending moment due to 1-cos gust encounters along the span of the wing for different gusts.

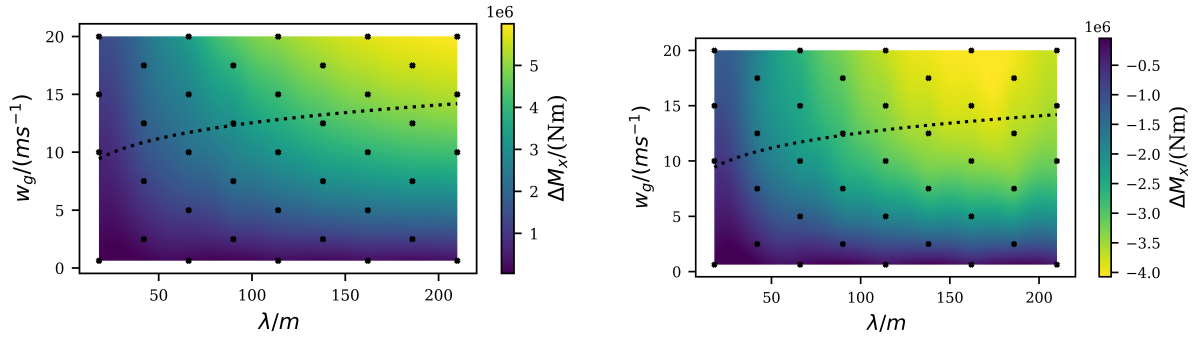

(a) Maximum wing bending moment at the wing root (b) Minimum wing bending moment at the wing root

Figure 7: Maximum and minimum wing bending moments due to 1-cos gust encounters at the wing root. Values are obtained by interpolation with radial basis functions.

distribution and the surface force distributions are found. First the time-linearized generalized forces and displacements are solved. Then, the latter allows to determine the time-linearized loads following Eq. (10) and the time-linearized surface pressure distribution analog to Eq. (9). After the multiplication of the transfer functions matrices with the gust signal in the frequency domain, the time-domain signals are obtained by the inverse Fourier transform.

The required simulations for the identification of the transfer function matrices are performed with a time step size of 0.0017s and 400 inner pseudo iterations. For identifying the linear response, the excitation amplitudes factors for the mode shapes are 10^{-5} for heave in meters and pitch in radians and 10^{-3} for the first wing bending for corresponding unity generalized mass. The distinction reflects the different scaling for the mode shapes as listed in table 2. The amplitude for the vertical gust input is 10^{-5}m/s. These amplitudes for each input signal are found by convergence analysis of the obtained transfer functions. Additionally, a convergence study for the time step size is conducted. The achieved frequency resolution in terms of the reduced frequency $\omega^* = 2\pi f L_{ref}/U_{ref}$, cf. Table 1, is less than $\Delta\omega^* = 4 \cdot 10^{-2}$. The maximum obtained reduced frequency is 50 which is a much higher value than the maximum required for the phenomena investigated in this work.

Fig. 9 shows the time signals of the time-linearized GAFs (dotted lines) in comparison to the nonlinearly obtained GAFs for multiple gust profiles. In the limit of very small gust amplitudes, the time-linearized results are expected to coincide with the nonlinear outcomes. Hence, this

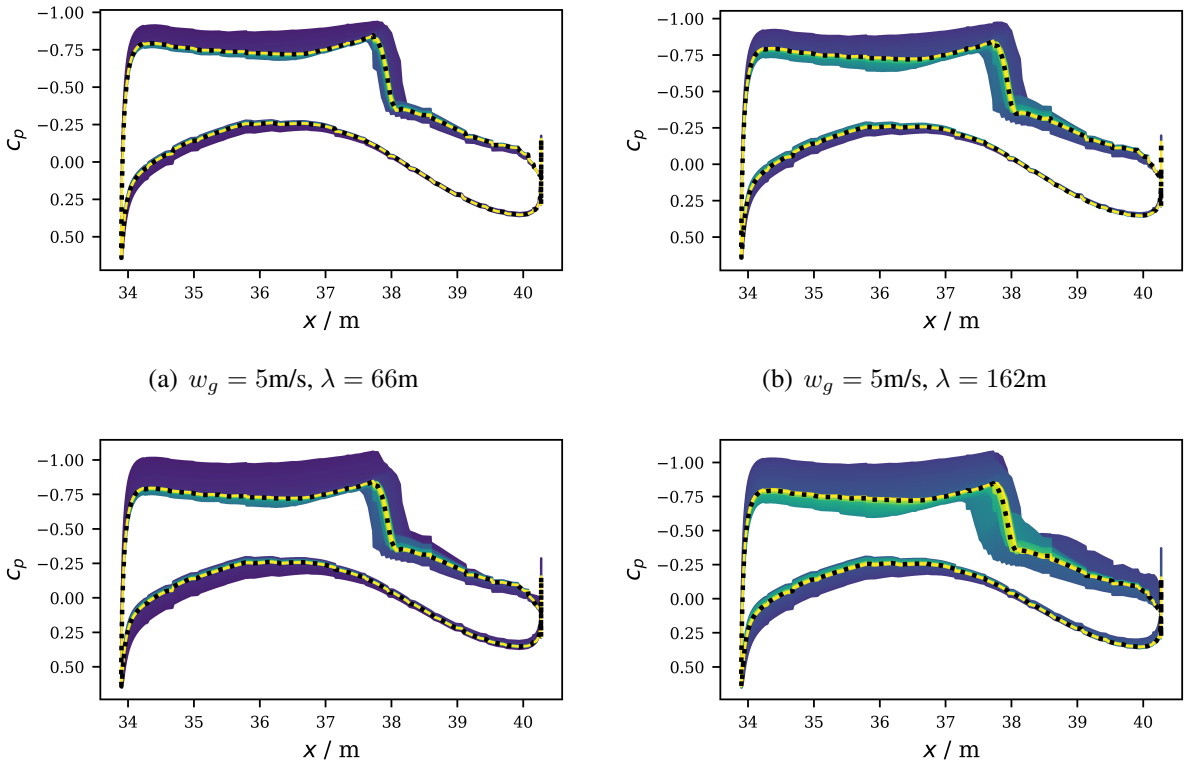

(a) $w_g = 5$m/s, $\lambda = 66$m

(b) $w_g = 5$m/s, $\lambda = 162$m

(c) $w_g = 10$m/s, $\lambda = 66$m

(d) $w_g = 10$m/s, $\lambda = 162$m

Figure 8: Time series of surface pressure along a cut of the wing at $y = 14.5$m due to 1-cos gust encounters plotted every $5 \cdot 10^{-3}$s for a period of 3s. Brighter colors are later in time and the steady state is plotted for reference (dashed black line)

can be verified for the gust amplitude of 0.625m/s in Fig. 9a which shows only small deviations from the nonlinear cases. With increasing gust amplitude, the signals start to diverge after the first ascent producing higher peaks, see Fig. 9b. Since the gust spectra change linearly with the gust amplitude, the time-linearized gust response varies linearly with the gust amplitude as well. Thus, the deviations including the decreased peaks stem from the nonlinearity of the fluid-structure interaction.

Fig. 10 compares the time-linearized wing bending moment envelopes (dotted lines) to the nonlinear load envelopes (solid lines) for different gust profiles. For the very low gust amplitude of 0.625m/s, cf. Fig. 10a, the time-linearized maximum and minimum loads agree very well with the nonlinear cases. However, the wing bending moment is overpredicted with increasing gust amplitude which is shown for the gust length of 114m in Fig. 10b. This overprediction is greater for the minimum wing bending moment at the wing root than for the maximum moment. Moreover, the inboard shift of the maximum moments with increasing gust amplitude is not captured. In Fig. 11 the contour plots for the maximum and minimum wing bending moments at the wing root obtained from the time-linearized loads are shown similar to the nonlinear cases in Fig. 7. For both the magnitudes grow with increasing gust amplitude and gust length. In comparison the maximum and minimum loads overshoot the nonlinear loads by a factor of 1.8 for mid-sized gust amplitudes and gust lenghts reaching a factor over 2 for greater values of the gust parameters. Moreover, the time-linearized results do not show the decrease in the minimum wing bending moment for gust lengths over 200m. Taken together, the time-linearized results cannot predict the nonlinear growth as it is found in Fig. 6 and Fig. 7 resulting

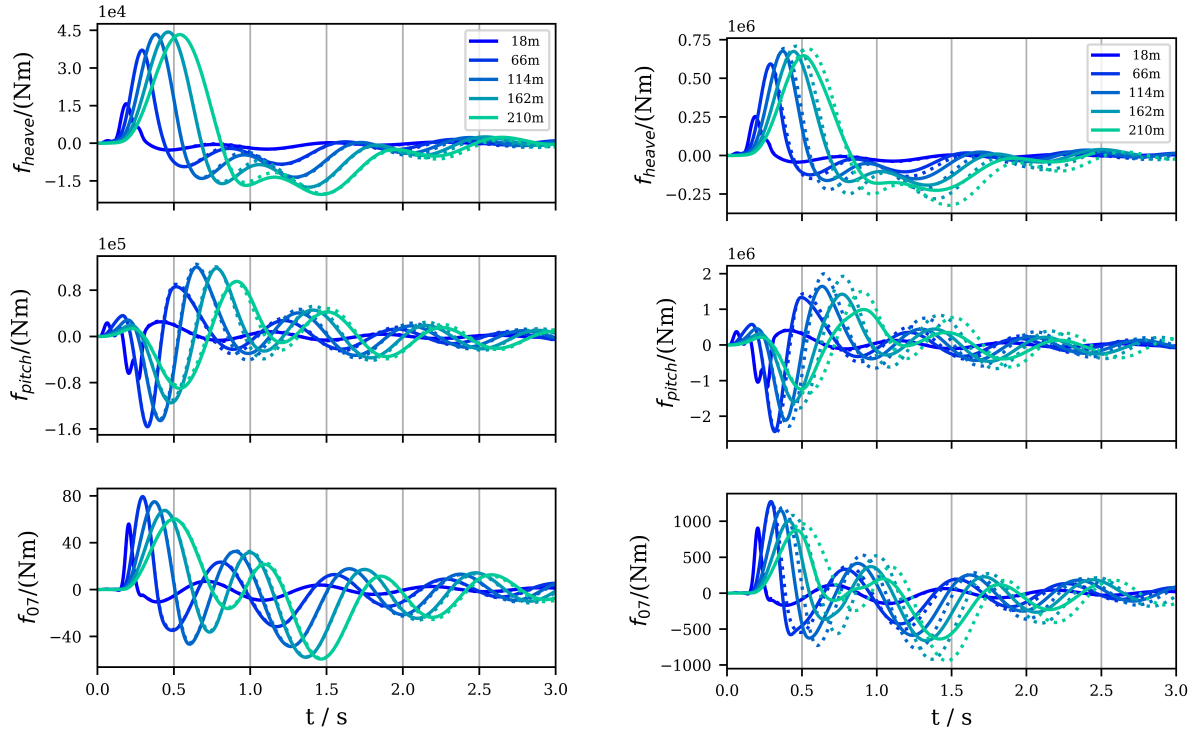

(a) $w_g = 0.625$m/s (b) $w_g = 10$m/s

Figure 9: Time signals of GAFs due to 1-cos gust encounters for different gust lengths comparing the nonlinear GAFs (solid) to the time-linearized GAFs (dotted).

in a significant overprediction of the wing bending moments. These findings are also observed by the direct comparison of the time-linearized and nonlinear wing bending moments at the wing root. Therefore, Fig. 12a shows the maximum wing bending moment for constant gust lengths of 66m and 162m with increasing gust amplitude. For gust amplitudes greater than 5m/s the time-linearized loads increase linearly while the nonlinear moments increase is attenuated. Accordingly, Fig. 12b shows the minimum wing bending for constant gust amplitudes of 10m/s and 15m/s. With increasing gust length the increase in the magnitude of the minium wing bending moment is significantly more attenuated for the nonlinear results.

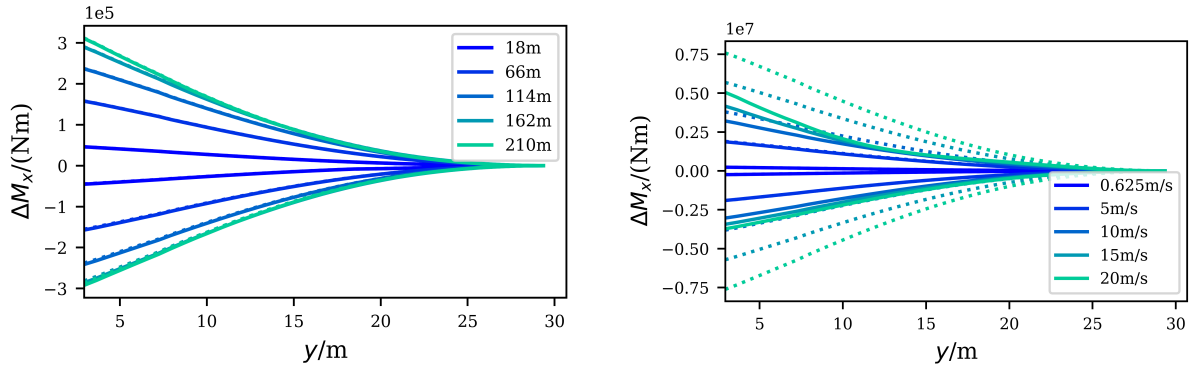

(a) $w_g = 0.625$m/s (b) $\lambda = 114$m

Figure 10: Loads envelopes of the wing bending moment due to 1-cos gust encounters along the span of the wing for different gusts comparing the nonlinear loads (solid) to the time-linearized loads (dotted).

In Fig. 13 the time-linearized surface pressure distribution is compared to the nonlinearly ob-

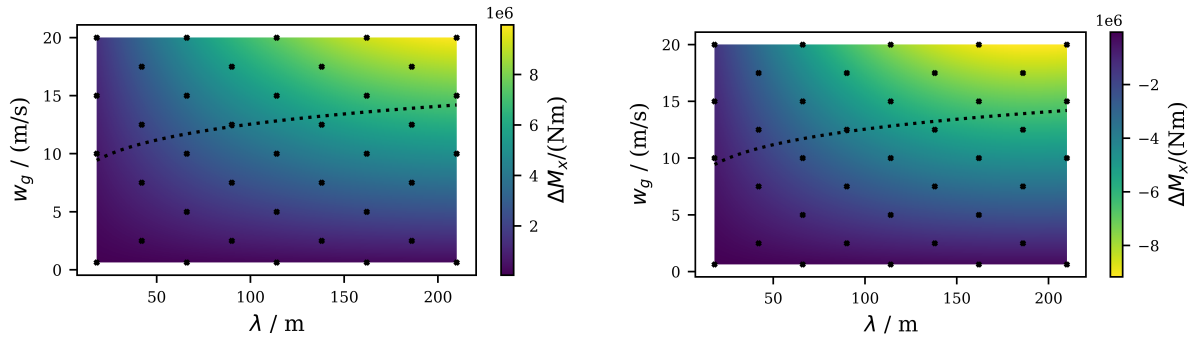

(a) Time-linearized maximum wing bending moment at the wing root

(b) Time-linearized minimum wing bending moment at the wing root

Figure 11: Time-linearized maximum and minimum wing bending moments due to 1-cos gust encounters at the wing root. Values are obtained by interpolation with radial basis functions.

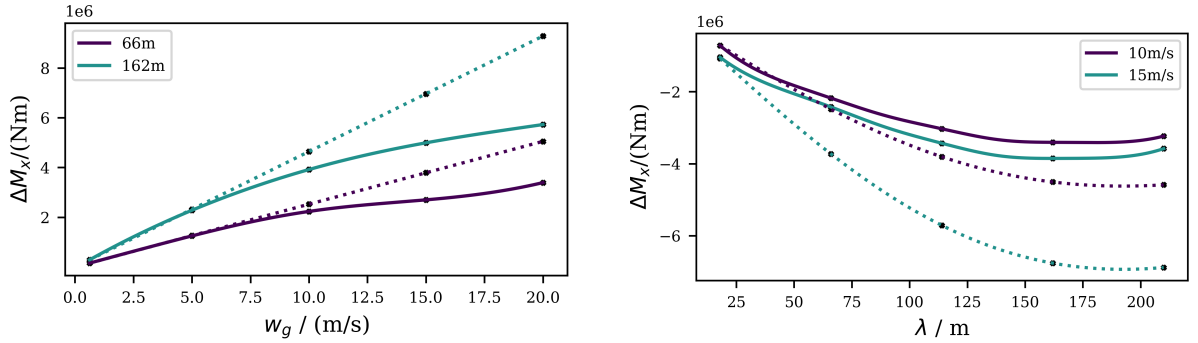

(a) Maximum wing bending moment at the wing root

(b) Minimum wing bending moment at the wing root

Figure 12: Maximum and minimum wing bending moments due to 1-cos gust encounters at the wing root comparing the nonlinear loads (solid) to the time-linearized loads (dotted). Values are obtained by interpolation with radial basis functions.

tained pressure for the gust amplitude of 0.625m/s and gust length of 18m. Due to the small amplitude, only the dynamic offset Δc_p is shown by subtracting the steady pressure distribution. Both time series show the similar behaviour as it is described for the nonlinear cases above. At first the pressure difference between the upper and lower surface increases and the recompression shock moves downstream which is found by the upwards peak in Δc_p. This is followed by an upstream motion passing the zero line and thus, the shock moves more upstream than in the steady state which is indicated by the downwards peak in Δc_p. Both time series return to zero after the excitation has passed. Due to the small gust amplitude and the low gust length, the overall shock motion is very small. The time-linearized time series agrees very well with the nonlinear time series and only minor deviations can be observed as it is expected in the limit of small amplitudes. The time-linearized gust response depends linearly on the gust amplitude and thus, from the time-linearized time-series in Fig. 13 it can be seen that with increasing gust amplitude the shock can only vary in strength. That is the peak can only accumulate higher with increasing gust amplitudes. Hence, the shock cannot move further up or down the stream as it is shown in Fig. 8. Consequently, the time-linearized surface pressure distribution will result unreasonable for greater gust amplitudes. This is shown in Fig. 14 for the gust cases of Fig. 8a and Fig. 8d. No increased shock motion can be observed and the shock strength is increased without physical meaning instead. A similar finding is shown in [20] for the CRM test case.

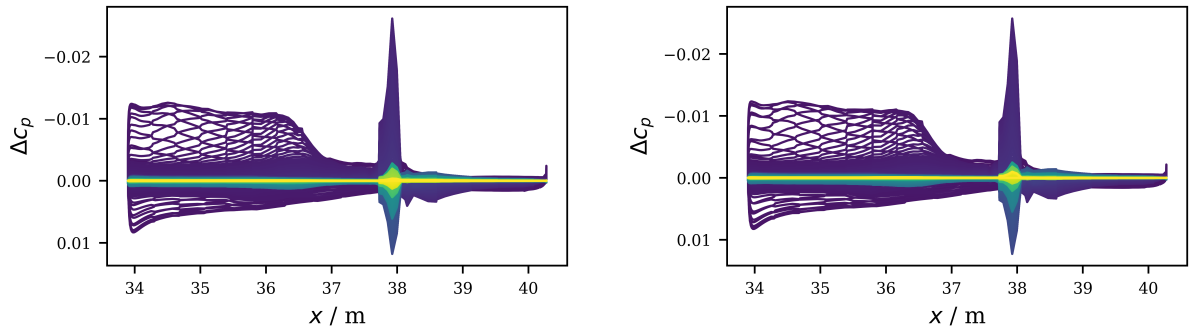

(a) Time-linearized

(b) Nonlinear

Figure 13: Time series of the dynamic offset of the surface pressure along a cut of the wing at $y = 14.5$m due to 1-cos gust encounter with $w_g = 0.625$m/s, $\lambda = 18$m and three mode shapes plotted every $5 \cdot 10^{-3}$s for a period of 3s. Brighter colors are later in time.

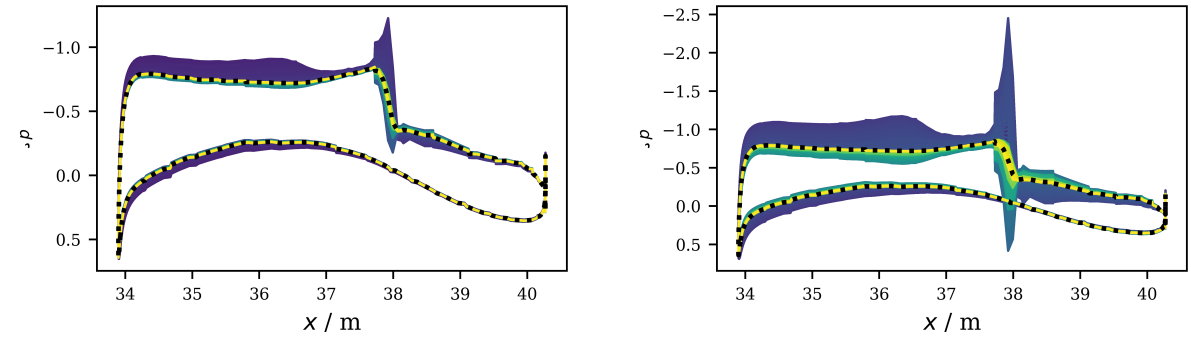

(a) $w_g = 5$m/s, $\lambda = 66$m

(b) $w_g = 10$m/s, $\lambda = 162$m

Figure 14: Time series of the time-linearized surface pressure along a cut of the wing at $y = 14.5$m due to 1-cos gust encounters plotted every $5 \cdot 10^{-3}$s for a period of 3s. Brighter colors are later in time and the steady state is plotted for reference (dashed black line)

This limited shock motion in the time-linearized surface pressure distribution suggests that the wing torsional moment is not captured correctly by the time-linearized results. Therefore, the wing torsional moment ΔM_y is analyzed by comparing it to the nonlinear results. Since the results in this paper do not comprise the wing's torsional degrees of freedom, the obtained wing torsional moments are expected to be higher than for an aricraft model with this degree of freedom. However, the computed torsional wing moment is a measure of the torque around the load reference axis acting on the wing caused by the aerodynamic and inertial forces. In Fig. 15 the time-linearized and nonlinear wing torsional moment at the wing root are compared by the contour plot of the relative error between both. The relative error is defined as

$$\frac{(\Delta M_{y,lin.} - \Delta M_{y,nonlin.})}{\Delta M_{y,nonlin.}}. \tag{11}$$

Thus, positive values of the relative error indicate overprediction by the time-linearized results and negative values show underprediction. From Fig. 15a it can be seen that the maximum wing torsional moment is overpredicted over the investigated gust parameter space reaching error values greater than 1. In contrast, for the minimum wing torsional moment in Fig. 15b underprediction is observed for wide areas of the gust parameter space including gust parameters which are required for the certification process.

The computational effort for the time-linearized approach in this study is considerably less than

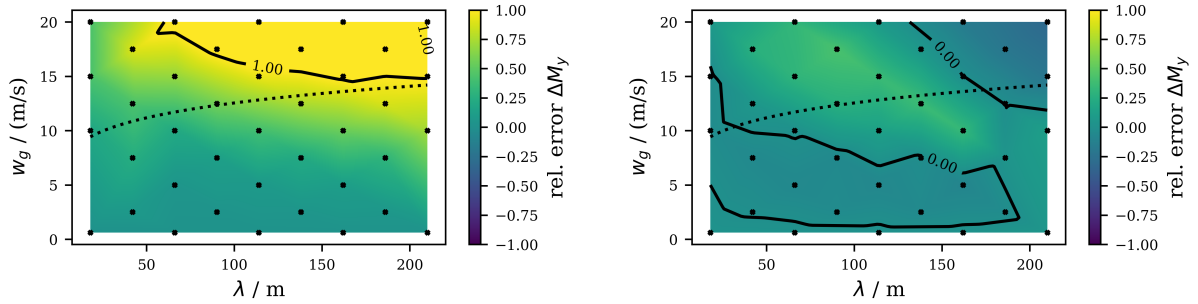

(a) Relative error of the maximum wing torsional moment at the wing root

(b) Relative error of the minimum wing torsional moment at the wing root

Figure 15: Relative errors of the time-linearized wing torsional moments due to 1-cos gust encounters at the wing root. Values are obtained by bilinear interpolation.

for the nonlinear analysis requiring four time-marching CFD solutions in order to approximate the time-linearized transfer function matrices. The subsequent computations in the frequency domain are negligible in terms of computational effort. In comparison, 39 unsteady aeroelastic simulations for the nonlinear analysis are performed.

4 CONCLUSION

Nonlinear and time-linearized gust load analysis based on RANS solutions are conducted covering a big part of the gust parameter space in order to quantify nonlinear effects in the gust load prediction. The nonlinear loads of the wing bending moment display a much attenuated increase with increasing gust amplitudes in contrast to the predicted the time-linearized loads. Moreover, the maximum magnitude of the minimum wing bending moment is not found for the greatest gust length as it is predicted by the time-linearized analysis. The analysis of the unsteady nonlinear surface pressure reveals a distinct shock motion due to the gust encounter. The shock's strength and its range of motion increases with increasing gust amplitude. Additionally, the shock's range of motion is significantly increased with increasing gust length. The time-linearized approach agrees very well with nonlinear loads for very small gust amplitudes but it clearly overpredicts the wing bending moment with increasing gust amplitude. Furthermore, the unsteady shock characteristcs of the time-linearized surface pressure is found to only match the cases for very small gust amplitudes. For greater gust amplitudes the time-linearized range of shock motion is limited to the small gust amplitude case producing unphysical peaks in the surface pressure distribution. This leads to overpredicted as well as underpredicted wing torsional moments and thus, no general conclusion over the possible conservatism introduced by the time-linearized loads can be reached.

5 REFERENCES

[1] Albano, E. and Rodden, W. P. (1969). A doublet-lattice method for calculating lift distributions on oscillating surfaces in subsonic flows. *AIAA Journal*, 7(2), 279–285. doi: 10.2514/6.1968-73.

[2] Thormann, R. and Widhalm, M. (2013). Linear-Frequency-domain predictions of Dynamic-Response data for viscous transonic flows. *AIAA Journal*, 51(11), 2540–2557.

[3] Kaiser, C., Thormann, R., Dimitrov, D., et al. (2015). Time-Linearized Analysis of Motion-induced and Gust-induced Airloads with the DLR TAU Code. In *Deutscher Luft- und Raumfahrtkongress (DLRK) 2015*.

[4] Kaiser, C., Friedewald, D., Quero-Martin, D., et al. (2016). Aeroelastic Gust Load Prediction based on time-linearized RANS solutions. In *Deutscher Luft- und Raumfahrtkongress (DLRK) 2016*.

[5] Weigold, W., Stickan, B., Travieso-Alvarez, I., et al. (2017). Linearized unsteady CFD for gust loads with Tau. In *International Forum on Aeroelasticity and Structural Dynamics (IFASD) 2017*.

[6] European Aviation Safety Agency (EASA) (2012). Certification specifications and acceptable means of compliance for large aeroplanes CS-25, amendment 12. Tech. rep., European Aviation Safety Agency (EASA).

[7] Newmark, N. M. (1959). A method of computation for structural dynamics. *Journal of Engineering Mechanics, Proceedings of the American Society of Civil Engineers*, 85, (EM3), 67–94.

[8] Schwamborn, D., Gerhold, T., and Heinrich, R. (2006). The DLR TAU-code: Recent applications in research and industry. In *European Conference on Computational Fluid Dynamics (ECCOMAS)*.

[9] Meinel, M. and Einarsson, G. O. (2010). The FlowSimulator framework for massively parallel CFD applications. In *PARA 2010*.

[10] Spalart, P. and Allmaras, S. (1992). A one-equation turbulence model for aerodynamic flows. In *30th Aerospace Sciences Meeting and Exhibit*. doi:10.2514/6.1992-439. AIAA-92-0439.

[11] Jameson, A. (1991). Time dependent calculations using multigrid, with applications to unsteady flows past airfoils and wings. In *10th Computational Fluid Dynamics Conference*. doi:10.2514/6.1991-1596. AIAA 91-1596.

[12] Hirt, C., Amsden, A. A., and Cook, J. L. (1974). An Arbitrary Lagrangian-Eulerian Computing Method for All Flow Speeds. *Journal of Computational Physics 14*, 227–253.

[13] de Boer, A., van der Schoot, M. S., and Bijl, H. (2007). Mesh deformation Based on Radial Basis Function Interpolation. *Computers and Structures*, 85(2), 784–795.

[14] Heinrich, R. (2014). Simulation of Interaction of Aircraft and Gust Using the TAU-Code. In *New Results in Numerical and Experimental Fluid Mechanics IX*, vol. 124 of *Notes on Numerical Fluid Mechanics and Multidisciplinary Design*. Springer International Publishing, pp. 503–511.

[15] Pototzky, A. and Perry, B. I. (1986). New and existing techniques of dynamic loads on response to impulsive excitation. *Journal of Aircraft*, 23, 340–347.

[16] Singh, R. and Baeder, J. D. (1996). The direct calculation of indicial lift response of a wing using computational fluid dynamics. In *AIAA Applied Aerodynamics Conference*.

[17] Vassberg, J., Dehaan, M., Rivers, M., et al. (2008). Development of a Common Research Model for Applied CFD Validation Studies. In *Guidance, Navigation, and Control and Co-located Conferences*. American Institute of Aeronautics and Astronautics. doi: 10.2514/6.2008-6919.

[18] Klimmek, T. (2014). Parametric Set-Up of a Structural Model for FERMAT Configuration for Aeroelastic and Loads Analysis. *Journal of Aeroelasticity and Structural Dynamics*, 3(2), 31–49.

[19] 4th AIAA Drag Prediction Workshop (2017). ftp://cmb24.larc.nasa.gov/outgoing/dpw4/dlr/solargrids.

[20] Bekemeyer, P., Ripepi, M., Heinrich, R., et al. (2019). Nonlinear unsteady reduced-order modelling for gust-load predictions. *AIAA Journal*, 57(5), 1839–1850.

COPYRIGHT STATEMENT